Ultra-broadband shortwave infrared emission under blue light excitation of Cr^{3+}/Ni^{2+} co-doped $Y_3Al_3MgSiO_{12}$ garnet phosphor through effective energy transfer and its application

Qian Zhang,[a] Xinyu Li,[a] Ziying Wang,[a] Qi Zhu,[b] Xuejiao Wang,[a*] Ji-Guang Li[c*]

[a]School of Materials and Environmental Engineering, Bohai University, Jinzhou, Liaoning 121013, China
[b]Key Laboratory for Anisotropy and Texture of Materials (Ministry of Education), School of Materials Science and Engineering, Northeastern University, Shenyang, Liaoning 110819, China.
[c]Research Center for Electronic and Optical Materials, National Institute for Materials Science, Tsukuba, Ibaraki 305-0044, Japan

*Corresponding author
Dr. Xuejiao Wang
Bohai University
Jinzhou, China
Tel: +86-416-3400708
E-mail: wangxuejiao@bhu.edu.cn

Dr. Ji-Guang Li
National Institute for Materials Science
Tsukuba, Japan
Tel: +81-29-860-4394
E-mail: li.jiguang@nims.go.jp

Abstract

Short-wave infrared (SWIR) phosphor-converted light-emitting diodes (pc-LEDs) are promising for biomedical and nondestructive applications. Still, their progress is constrained by the lack of efficient, ultra-broadband phosphors excitable by low-cost blue LEDs. Cr^{3+}-activated materials exhibit strong blue light excitation, but their emission is primarily confined to the NIR-I region. In contrast, Ni^{2+} has the potential to achieve SWIR emission, yet suffers from weak absorption in the blue-light region. In this study, $Y_3Al_3MgSiO_{12}$: Ni^{2+} and $Y_3Al_3MgSiO_{12}$: Cr^{3+}-Ni^{2+} phosphors were synthesized. Compared to previous reports, the $Y_3Al_3MgSiO_{12}$: Cr^{3+}-Ni^{2+} phosphor in this study achieved three significant advancements. (1) Efficient energy transfer from Cr^{3+} to Ni^{2+} was achieved (η=91.6%), resulting in a 10.45-fold enhancement of SWIR emission intensity upon 438 nm blue-light excitation, and the optimal excitation wavelength was shifted into the blue-light region. (2) Ultra-broadband continuous emission spanning the NIR-I to NIR-III regions, with an exceptionally wide FWHM (185+311 nm) was achieved in this phosphor. (3) Remarkably high thermal stability was achieved for the NIR-II-III emission, in a region where strong electron-phonon coupling and poor thermal stability are typically observed. The underlying mechanism was elucidated through analysis of the crystal structure rigidity and the Huang-Rhys factor (S). A SWIR pc-LED device was further fabricated by integrating the phosphor with a 450 nm blue LED chip, confirming its application potential in covert information recognition and nondestructive detection scenarios. This study not only introduces a broadband SWIR-emitting material system excitable by blue light but also provides a novel strategy for developing efficient and thermally stable SWIR phosphors.

***Keywords*:** SWIR phosphor, ultra-broadband emission, garnet, Cr^{3+}-Ni^{2+} co-doping

1. Introduction

Shortwave infrared (SWIR) luminescence technology offers deep tissue penetration, no autofluorescence interference, and a high degree of compatibility with characteristic absorption peaks of organic molecules (such as O-H and C-H), demonstrating unique advantages in fields such as in vivo imaging, non-destructive testing, and photodynamic therapy [1-2]. The NIR region is conventionally categorized into NIR-I (700-1000 nm), NIR-II (1000-1500 nm), and NIR-III (1500-1850 nm), while the SWIR spectrum spans the 900-1700 nm range [3]. Compared with traditional tungsten halogen lamps, shortwave infrared phosphor-converted light-emitting diodes (SWIR pc-LEDs) are regarded as a core technology for the next generation of SWIR light sources [4]. They offer advantages such as low cost, miniaturization, high power efficiency, and long lifespan [5]. Typically, SWIR pc-LEDs consist of an InGaN blue LED chip combined with broadband SWIR-emitting phosphor materials. The broadband emission can effectively span the NIR-II to NIR-III ranges (1000-1700 nm), making them suitable for applications such as high-resolution vascular imaging and deep tumor detection [6-7]. Therefore, developing novel phosphors capable of both blue-light excitation and ultra-broadband SWIR emission is key to expanding the application boundaries of SWIR pc-LEDs.

The dopant activators in SWIR phosphors are generally classified as trivalent lanthanide ions and transition metal ions. In contrast to the 4*f*-4*f* transitions of trivalent lanthanide ions, transition metal ions possess 3*d*-3*d* spin-allowed transitions, thereby exhibiting excellent broadband NIR emission performance [8]. As a result, transition metal ions are more suitable for doping into host matrices to design SWIR phosphors.

Owing to its broad and strong absorption in the blue-light region, Cr^{3+} stands out among transition metal ions as a highly compatible activator for InGaN blue-light chips [9-12]. However, the emission of Cr^{3+} is predominantly confined to the NIR-I region, and extending its emission wavelength into the NIR-II/III region remains a significant challenge [13]. Fortunately, Ni^{2+} ions with a $3d^8$ electronic configuration have shown great potential for ultra broadband SWIR emission in the NIR-II region under weak octahedral crystal field environments (Dq/B < 1.7). This makes Ni^{2+} an ideal luminescent center, a feature already validated in phosphors such as $ZnGa_2O_4$: Ni^{2+}, $MgTi_2O_5$: Ni^{2+}, and $Mg_3Ga_2GeO_8$: Ni^{2+} [14-16]. However, it should be noted that in existing studies, Ni^{2+} excitation primarily occurs in the ultraviolet region, while its absorption in the blue-light region is relatively weak, preventing efficient excitation by blue-light chips. Although some studies have developed single Ni^{2+}-activated NIR phosphors that can be excited by blue light, such as $Y_3Al_2Ga_3O_{12}$: Ni^{2+} and Mg_2SnO_4: Ni^{2+} [17-19], their spectral overlap with the blue-light region remains low. Additionally, Ni^{2+}-activated NIR phosphors typically exhibit large Stokes shifts, resulting in relatively low photoluminescence efficiency. To address this issue, a Cr^{3+}-Ni^{2+} co-doping strategy has been proposed, which enhances Ni^{2+} SWIR emission through energy transfer from Cr^{3+}, thereby improving photoluminescence efficiency. Cr^{3+} is chosen as a sensitizer not only because it efficiently absorbs blue light but also because its NIR emission strongly overlaps with the Ni^{2+} absorption band. This advantage has been validated in systems such as $MgGa_2O_4$: Cr^{3+}-Ni^{2+} and MgO: Cr^{3+}-Ni^{2+} [20-21]. However, the development of Cr^{3+}-Ni^{2+} co-doped SWIR phosphors with efficient energy transfer, excellent photoluminescence performance, and good thermal stability remains a significant challenge.

In this study, we report a novel broadband SWIR phosphor, $Y_3Al_3MgSiO_{12}$: Ni^{2+}, exhibiting ultra-broadband emission spanning 1000-1650 nm. Notably, it is excitable by visible light (λ_{ex} = 408 nm), rather than UV radiation. Diverging from previous $Y_3Ga_3MgSiO_{12}$: Ni^{2+} report, more stable and economically viable Al was employed to substitute Ga. This substitution not only enhances the rigidity of the crystal structure, thereby improving thermal stability but also significantly reduces raw material costs. Furthermore, through a Cr^{3+}-Ni^{2+} co-doping strategy, $Y_3Al_3MgSiO_{12}$: Cr^{3+}- Ni^{2+} demonstrates ultra broadband SWIR emission (FWHM =185+311 nm) spanning 600-1650 nm under 438 nm blue-light excitation, covering the spectral regions from NIR-I to NIR-III. The phosphor exhibits highly efficient energy transfer from Cr^{3+} to Ni^{2+} (η = 91.6%) and excellent thermal stability, with NIR-II-III emission intensities maintaining 56% of their room-temperature values at 373 K, respectively. The influence of the Huang-Rhys factor and the rigidity of the crystal structure on this thermal stability is also discussed. Finally, a SWIR pc-LED was fabricated by coupling the $Y_3Al_3MgSiO_{12}$: Cr^{3+}-Ni^{2+} phosphor with a commercial 450 nm InGaN blue LED chip. The resulting device exhibited promising performance, demonstrating the potential for applications in covert object identification and non-contact, nondestructive detection scenarios.

2. Results and Discussion

2.1. Structure and Composition

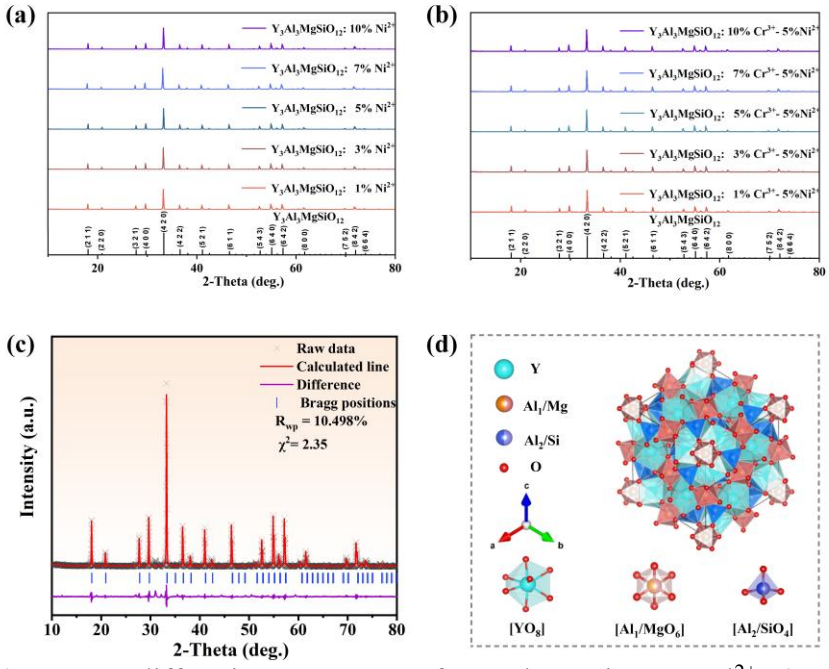


Fig. 1 (a-b) X-ray diffraction patterns of $Y_3Al_3MgSiO_{12}$: xNi^{2+} (x = 1%-10%), $Y_3Al_3MgSiO_{12}$: 5% Ni^{2+}-yCr^{3+} (y = 1%-10%). (c) Rietveld refinement results of $Y_3Al_3MgSiO_{12}$: 5% Ni^{2+}-5% Cr^{3+}. (d) Crystal structure of $Y_3Al_3MgSiO_{12}$.

Fig. 1(a-b) illustrates the powder X-ray diffraction patterns of $Y_3Al_3MgSiO_{12}$: xNi^{2+} (x = 1%-10%) and $Y_3Al_3MgSiO_{12}$: 5% Ni^{2+}-yCr^{3+} (y = 1%-10%) phosphors. The diffraction peaks are following the standard card of $Y_3Al_5O_{12}$ (PDF#97-017-0157), thereby indicating that all the synthesized samples are pure phases. To elucidate the impact of Ni^{2+} and Cr^{3+} doping, the Rietveld refinement of $Y_3Al_3MgSiO_{12}$: 5% Ni^{2+}-5% Cr^{3+} are illustrated in Fig. 1(c). Table S1-S2 provide detailed information regarding the processing and refining parameters for the aforementioned samples, along with the atomic number fraction coordinates and atomic occupancies of the samples. Fig. 1(d) illustrates the crystal structure of the compound $Y_3Al_3MgSiO_{12}$, which exhibits a typical $A_3B_5O_{12}$-type

garnet structure and belongs to the space group I*a*-3*d*. In this structure, the Y^{3+}, Al_1^{3+}/Mg^{2+}, and Al_2^{3+}/Si^{4+} cations are coordinated to 8, 6, and 4 O^{2-} ions, respectively, to form dodecahedral, octahedral, and tetrahedral structures [22]. In a six-coordinate environment, the ionic radii of Ni^{2+}, Al^{3+}, Mg^{2+}, and Cr^{3+} are 0.69, 0.535, 0.72, and 0.615 Å, respectively. It is predicted that when Ni^{2+} and Cr^{3+} ions are doped into the matrix $Y_3Al_3MgSiO_{12}$, Ni^{2+} will take the place of the Mg^{2+} ion due to the similarity of ionic radii and valence, while Cr^{3+} will occupy the position of Al^{3+} ion. Ionic substitution behavior is primarily governed by the charge compatibility and ionic radius matching between the dopant and host cations. Among these factors, the ionic radius difference parameter (D_r) serves as a critical criterion for evaluating the feasibility of substitution. It can be calculated using the following empirical equation:

$$D_r = \frac{|R_r - R_d|}{R_r} \times 100\% \quad (1)$$

Here, R_d and R_r represent the ionic radii of the dopant and the substituted host cation, respectively. Generally, when the ionic radius difference D_r is below 30%, ionic substitution is considered feasible within the crystal structure [23]. In the case of $Y_3Al_3MgSiO_{12}$, the D_r values of Ni^{2+} relative to the Mg^{2+} and Al^{3+} sites are 4.17% and 28.97%, respectively, indicating a stronger preference for substitution at the Mg^{2+} site due to the better ionic radius match. In contrast, Cr^{3+} exhibits D_r values of 14.58% and 14.95% for the Mg^{2+} and Al^{3+} sites, respectively. Thermoluminescence (TL) measurements can be employed to characterize the distribution of charge traps, where the peak position reflects

the trap depth and the peak area corresponds to the trap concentration [24]. To further investigate the site occupancy behavior of the dopant ions, TL spectra were recorded under 260 nm excitation for pre-irradiated $Y_3Al_3MgSiO_{12}$ host and $Y_3Al_3MgSiO_{12}$: 5% Ni^{2+}-5% Cr^{3+} samples (Fig. S1). Both samples showed no distinct TL peaks, suggesting that no significant charge traps were introduced during the doping process. Based on the principle of charge balance, Cr^{3+} is more likely to occupy the Al^{3+} sites preferentially.

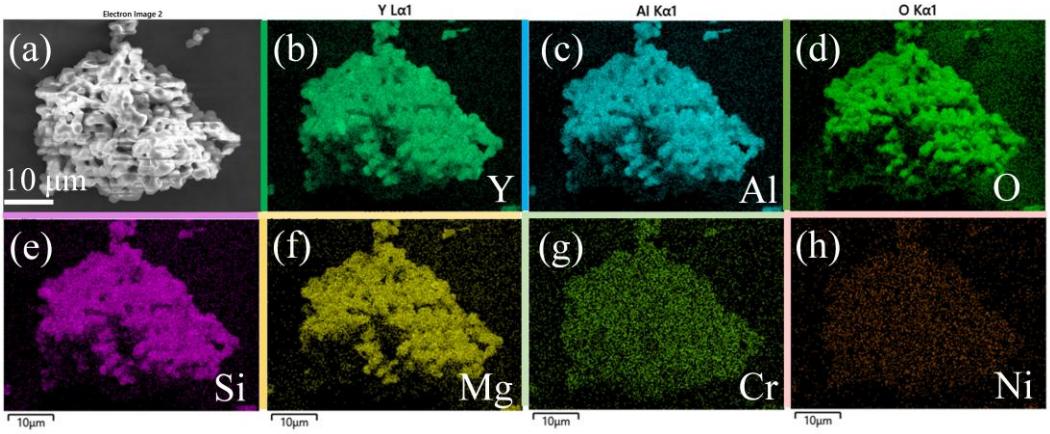


Fig. 2(a) SEM image and (b-h) the elemental mapping images of the as-prepared $Y_3Al_3MgSiO_{12}$: 5% Ni^{2+}-5% Cr^{3+} phosphor.

Fig. 2(a) depicts the element mapping images of $Y_3Al_3MgSiO_{12}$: 5% Ni^{2+}-5% Cr^{3+} in a scanning electron microscope (SEM), and Fig. 2 (b-h), demonstrates that all elements of Y, Al, Mg, Si, O, Cr, and Ni are distributed uniformly throughout the particles, with no evidence of element aggregation or phase separation.

2.2. Luminescence Properties

2.2.1. Cr^{3+}/Ni^{2+} Mono-Doped $Y_3Al_3MgSiO_{12}$

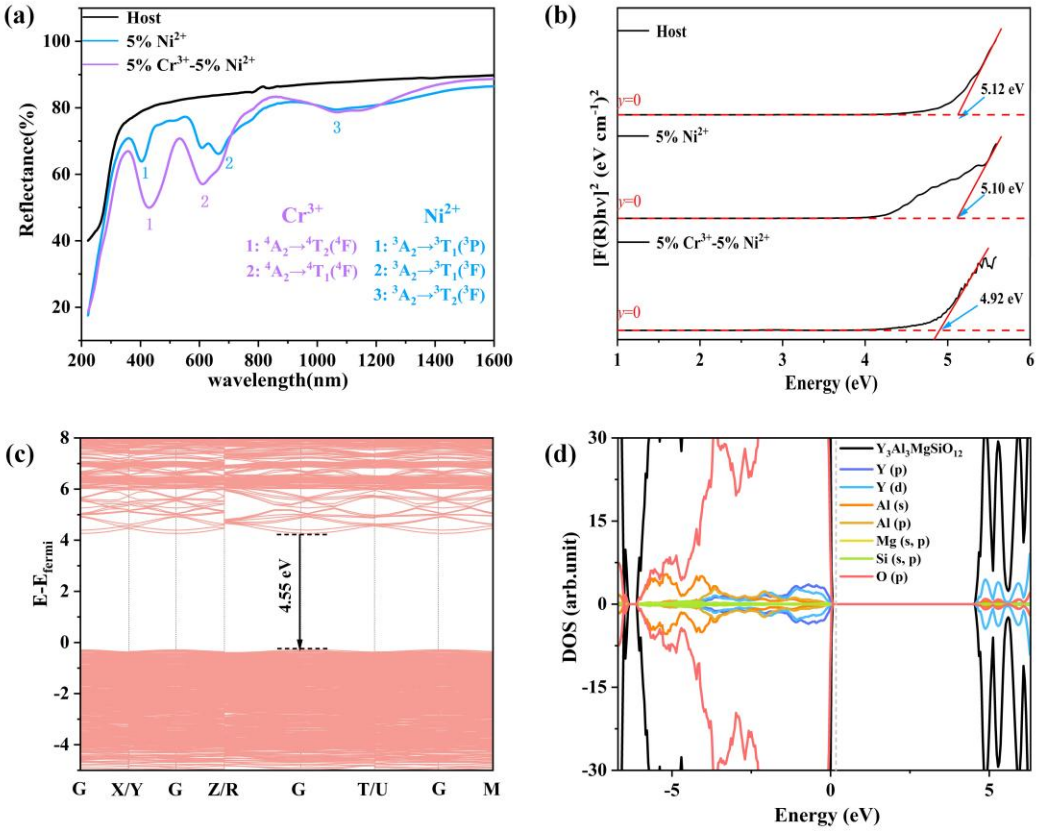


Fig. 3. (a) The DRS of $Y_3Al_3MgSiO_{12}$: xNi^{2+} (x = 0, 5%), $Y_3Al_3MgSiO_{12}$: 5% Ni^{2+}-5% Cr^{3+}. (b) Band gap determination, where $(F(R)*h\nu)^2$ is a function of photon energy. (c-d) The band structure and density of states of $Y_3Al_3MgSiO_{12}$ host.

Fig. 3(a) illustrates the diffuse reflectance (DR) spectra of $Y_3Al_3MgSiO_{12}$: xNi^{2+} (x = 0%, 5%) and $Y_3Al_3MgSiO_{12}$: 5%Ni^{2+}-5% Cr^{3+} phosphors. Multiple absorption peaks are observed in the ultraviolet-visible-near infrared region. A comparison of the DR spectra of the $Y_3Al_3MgSiO_{12}$ matrix with those of $Y_3Al_3MgSiO_{12}$: 5% Ni^{2+}. The absorption peaks are located at 408 nm, 668 nm, 1064 nm, and 464 nm, respectively, and can be classified as three main peaks and a weak absorption peak. These transitions are derived from the spin-allowed $^3A_2 \rightarrow {}^3T_1$ (^3P), $^3A_2 \rightarrow {}^3T_1$ (^3F), and $^3A_2 \rightarrow {}^3T_2$ (^3F) electronic transitions and the spin-forbidden $^3A_2 \rightarrow {}^3T_1$ (^1D) electronic transitions of Ni^{2+} [25]. In comparison to the DR spectrum of $Y_3Al_3MgSiO_{12}$: 5% Ni^{2+}, the compound $Y_3Al_3MgSiO_{12}$: 5% Ni^{2+}-5%

Cr^{3+} reveals two prominent absorption peaks at 438 nm and 590 nm, which arise from the electronic transitions of Cr^{3+}: $^4A_2(^4F) \rightarrow {}^4T_1(^4F)$ and $^4A_2(^4F) \rightarrow {}^4T_2(^4F)$, respectively [26]. The value of the band gap (E_g) can be calculated according to the following formula:

$$F(R_\infty) = \frac{(1-R)^2}{2R} \quad (2)$$

$$[h\nu F(R_\infty)]^n = A(h\nu - E_g) \quad (3)$$

Here, A is a proportionality constant, $h\nu$ denotes the energy of a single photon, and $F(R_\infty)$ is the Kubelka-Munk function, which is proportional to the absorption coefficient. The exponent n reflects the nature of the band gap: n = 1/2 corresponds to indirectly allowed, n = 2 to directly allowed, n = 3/2 to indirectly forbidden, and n = 3 to directly forbidden [27]. In this work, the $Y_3Al_3MgSiO_{12}$ phosphor has a direct band gap type with an n value of 2. Fig. 3(b) shows the relationship between $[h\nu F(R_\infty)]^2$ and $h\nu$. Through the analysis of diffuse reflectance data, we ascertain that the optical band gaps of $Y_3Al_3MgSiO_{12}$, $Y_3Al_3MgSiO_{12}$: 5%Ni^{2+}, and $Y_3Al_3MgSiO_{12}$: 5% Ni^{2+}-5% Cr^{3+} are 5.12 eV, 5.10 eV, and 4.92 eV, respectively.

Fig. 3(c-d) presents the electronic band structure of $Y_3Al_3MgSiO_{12}$ and the projected density of states (PDOS) of its constituent elements Y, Al, Mg, Si, and O. It can be observed that the material exhibits a direct bandgap, with a calculated bandgap value of 4.55 eV. The calculated bandgap is closely related to the bond strength between atoms and their valence electrons. A stronger covalent character implies greater overlap between valence electron orbitals, resulting in more localized electron cloud density and tighter bonding, which in turn leads to the formation of stronger chemical bonds [28]. Typically, an increase in covalent bond strength widens the energy gap between the valence and conduction bands, resulting in a larger bandgap [29]. A larger bandgap not only reflects stronger covalency but also contributes to enhanced luminescence intensity. Additionally,

materials with smaller bandgaps are more susceptible to thermally activated photoionization processes, which exacerbate luminescence quenching [30]. Therefore, the material with relatively large bandgaps are expected to exhibit better thermal stability upon Ni^{2+}/Cr^{3+} doping. Further analysis of the DOS reveals that the valence band is primarily composed of O (p) states, accompanied by minor contributions from the Al (s) and Al (p) states, while the conduction band is predominantly derived from the Y (d) states.

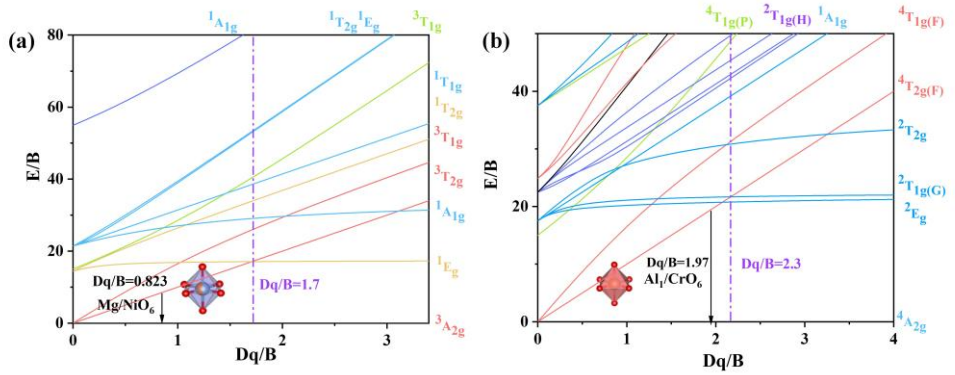


Fig. 4. The Tanable - Sugano diagram of (a) $Y_3Al_3MgSiO_{12}$: Ni^{2+} and (b) $Y_3Al_3MgSiO_{12}$: Cr^{3+}.

The emission position of dopant ions at the luminescent center largely depends on the crystal field environment of the host lattice. Therefore, assessing the crystal field strength provides valuable insights into the luminescent behavior of Ni^{2+} and Cr^{3+} ions within the $Y_3Al_3MgSiO_{12}$ matrix. The crystal field environment of Ni^{2+} and Cr^{3+} ions in an octahedral field can be evaluated using the Tanabe-Sugano diagrams for $3d^8$ and $3d^3$ configurations in Fig. 4(a-b). The crystal field strength (*Dq/B*) for $Y_3Al_3MgSiO_{12}$: 5% Ni^{2+} and $Y_3Al_3MgSiO_{12}$: 1% Cr^{3+} phosphors can be determined using the following two equations:

$$Dq = \frac{v1}{10} \quad (4)$$

$$B = \frac{(v3 - 2v1)(v3 - v1)}{3(5v3 - 9v1)} \quad (5)$$

Here, *Dq* stands for the crystal field parameter, and *B* refers to the Racah parameter. The terms v_1 and v_3 refer to the energy values of the transitions $^3A_2 \rightarrow {}^3T_2$ (F) and $^3A_2 \rightarrow {}^3T_1$ (P) for Ni^{2+} ions, and $^4A_2 \rightarrow {}^4T_1$ (F) and $^4A_2 \rightarrow {}^4T_2$ (F) for Cr^{3+} ions. According to crystal field theory, the crystal field can be classified as strong or weak based on the relative energy of the $^3T_2$ and ^1E levels for Ni^{2+} ions: a weak crystal field is indicated when $^3T_2$ is the first excited state transitioning to the ground state $^3A_2$ (Dq/B < 1.7). In contrast, a strong crystal field occurs when ^1E is the first excited state (Dq/B > 1.7) [31]. For Cr^{3+} ions, the field strength is determined by the relative energies of $^4T_2$ and ^2E, a weak field is present when $^4T_2$ is the first excited state transitioning to the ground state $^4A_2$ (Dq/B < 2.3), and a strong field when ^2E is the first excited state (Dq/B > 2.3) [32]. Thus, the calculated crystal field strengths Dq/B for $Y_3Al_3MgSiO_{12}$: 5% Ni^{2+} and $Y_3Al_3MgSiO_{12}$: 1% Cr^{3+} phosphors are 0.823 (< 1.7) and 1.97 (< 2.3), respectively, indicating that both Ni^{2+} and Cr^{3+} ions in these phosphors are situated in a weak crystal field.

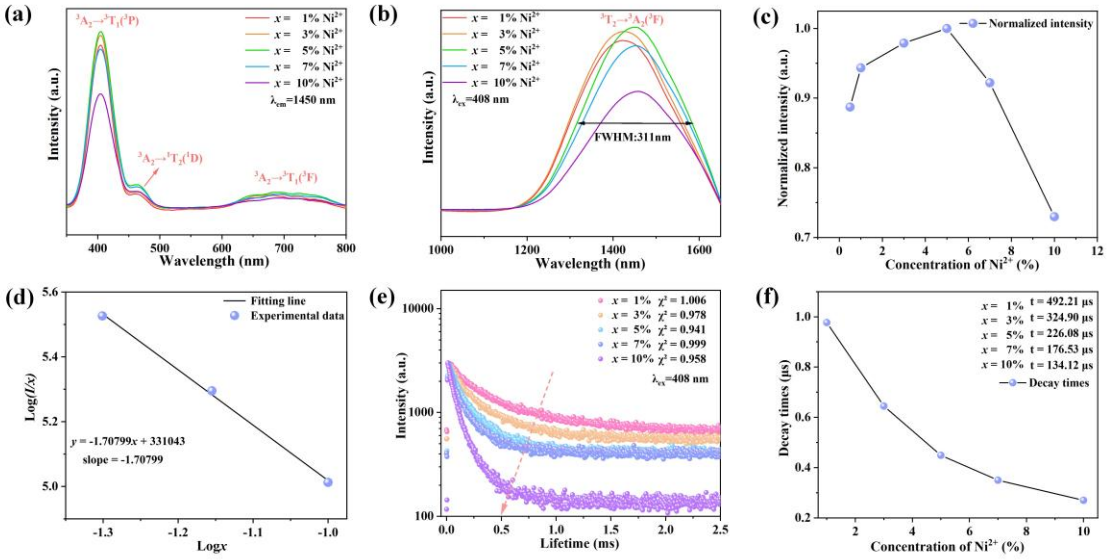


Fig. 5. (a-b) Excitation and emission spectra of $Y_3Al_3MgSiO_{12}$: xNi^{2+} (x = 1%-10%) phosphors. (c) The dependence of emission intensity on Ni^{2+} concentration. (d) The fitting diagram of the concentration quenching mechanism. (e) Decay curve for the main

emission of the phosphors. (f) Dependence of average lifetime on Ni^{2+} concentration.

The excitation and emission spectra of $Y_3Al_3MgSiO_{12}$: xNi^{2+} (x = 1%-10%) phosphors are illustrated in Fig. 5(a-b). Upon monitoring at a wavelength of 1450 nm, three excitation bands at 408 nm, 464 nm, and 668 nm are observed to align with the absorption bands evident in the DR spectrum (Fig. 3(a)). These transitions are attributed to the $^3A_2$ (F) → $^3T_1$ (^{3}P), $^3A_2$ (F) → $^1T_2$ (D), and $^3A_2$ (F) → $^3T_1$ (F) transitions of Ni^{2+} [33]. Due to the spin-allowed $^3T_2$ (^{3}F) to $^3A_2$ (^{3}F) transition of Ni^{2+} ions, $Y_3Al_3MgSiO_{12}$: Ni^{2+} has a wide emission band in the wavelength range of 1000-1700 nm under the excitation of 408 nm, and its FWHM value reaches 311 nm. The modulation of crystal field splitting induced by increasing Ni^{2+} concentration has a substantial effect on the luminescence properties. The emission in Fig. 5(b) undergoes a noticeable redshift, with the peak wavelength shifting from 1422 nm to 1460 nm as the Ni^{2+} content increases. This phenomenon stems from the changes in the crystal field splitting around the Ni^{2+} ions, and can be analyzed using the following formula:

$$Dq = \frac{Ze^2r^2}{6R^5} \quad (6)$$

In this formula, Z and e denote the charge numbers of the anion and electron, respectively, r and R represent the radius of the d-orbital wave function and the distance between the central ion and the ligand. As the concentration of Ni^{2+} doping increases, the crystal field splitting around it intensifies. This not only reduces the influence of Ni^{2+} on the lowest 3d states but also weakens the crystal field strength surrounding Ni^{2+}. Consequently, this alters the energy levels of $^3T_1$ (^{3}P) and $^3T_1$ (^{3}F), leading to the observed redshift in the

normalized emission spectrum [34].

Fig. 5(c) reveals a strong concentration-dependent trend in the emission intensity of $Y_3Al_3MgSiO_{12}$: Ni^{2+}. The emission intensity increases with Ni^{2+} content, reaches a maximum at x = 5%, and then decreases due to concentration quenching. As the Ni^{2+} concentration increases, the probability of energy transfer between Ni^{2+} ions in the $Y_3Al_3MgSiO_{12}$ host correspondingly increases. Given that the excitation and emission spectra of $Y_3Al_3MgSiO_{12}$: Ni^{2+} phosphors do not overlap, the primary form of the energy transfer mechanism is determined by the critical distance (R_c) between Ni^{2+} ions [35]. When the value of R_c is equal to or less than 0.5 nm, the primary form of energy transfer is exchanged interaction. However, when R_c exceeds 0.5 nm, the dominant mechanism shifts to multipolar interaction. To comprehend the concentration quenching process of $Y_3Al_3MgSiO_{12}$: Ni^{2+}, it is essential to employ the following formula to calculate R_c:

$$R_C = 2\left(\frac{3V}{4\pi x_c N}\right)^{1/3} \quad (7)$$

In this equation, N represents the number of cations in the cell, V represents the cell volume, and x_c represents the optimal nickel ion concentration in $Y_3Al_3MgSiO_{12}$. For $Y_3Al_3MgSiO_{12}$.: 5% Ni^{2+}, R_c was calculated using N = 8, V = 1727.212 $Å^3$, and x_c = 0.05. According to the formula, it can be estimated that the R_c value is approximately 2.02 nm greater than 0.5 nm, indicating that the primary mechanism of concentration quenching is multipolar interaction. To analyze the mechanism and type of multipolar interaction between Ni^{2+} ions in $Y_3Al_3MgSiO_{12}$, the following equation can be used to analyze according to Dexter's theoretical hypothesis [36-37]:

$$\frac{I}{x} = k[1 + \beta(x)^{\theta/3}]^{-1} \quad (8)$$

In this equation, the variable *I* represents the photoluminescence intensity detected in the sample, and *x* represents the concentration of Ni^{2+} ion. For a given host lattice, the constants β and k are fixed, while the parameter θ determines the type of multipolar interactions. Specifically, θ = 3, 6, 8, and 10 correspond to the non-radiative energy transfer between neighboring ions, dipole-dipole, dipole-quadrupole, and quadrupole-quadrupole interactions, respectively [38]. The log-log plot of log (*I/x*) versus log (*x*) is shown in Fig. 5(d), and this relationship exhibits a linear dependence, with a fitted slope of approximately -1.70799. The calculation result of θ is 5.12, which can be approximated as 6. Therefore, the quenching process is primarily dominated by the non-radiative energy transfer caused by the dipole-dipole multipole interaction.

Fig. 5(e) shows the decay curves of the 1450 nm SWIR emission of $Y_3Al_3MgSiO_{12}$: $x$$Ni^{2+}$ (x = 1%-10%) phosphors under 408 nm excitation. The decay curves can be fitted by a double exponential function [39].

$$I = A_1 \exp\left(-\frac{t}{\tau_1}\right) + A_2 \exp\left(-\frac{t}{\tau_2}\right) \quad (9)$$

$$\tau^* = \frac{A_1\tau_1^2 + A_2\tau_2^2}{A_1\tau_1 + A_2\tau_2} \quad (10)$$

In Eq. (9), A_1 and A_2 are fixed constants, and τ_1 and τ_2 represent the lifetime of the exponential component, the fluorescence intensity at time *t* is denoted by *I*. Based on the following Eq. (10), the corresponding average lifetimes were calculated to be 492.21, 324.90, 226.08, 176.53, and 134.12 μs, respectively. The PL intensity of the Ni^{2+}-doped sample reaches its maximum at a doping concentration of 5%. However, the

luminescence lifetime monotonously decreases with increasing Ni^{2+} concentration. This contrasting phenomenon can be attributed to the enhancement of non-radiative relaxation processes [40]. The relationship between fluorescence lifetime (τ), radiative relaxation rate (W_R), and non-radiative relaxation rate (W_{NR}) can be expressed as follows:

$$\frac{1}{\tau} = W_R + W_{NR} \quad (11)$$

With increasing Ni^{2+} concentration, the probability of energy transfer between adjacent Ni^{2+} ions as well as between Ni^{2+} ions and luminescence quenching centers increases, which significantly enhances the occurrence of non-radiative relaxation processes and consequently shortens the luminescence lifetime [41]. The specific values of the fitting results are shown in Table 1. Fig. 5(f) shows the correlation between the fluorescence lifetime and the change of *x* doping concentration.

Table 1. The fitted fluorescence decay results for the 1450 nm emission (λ_{ex}= 408 nm) of $Y_3Al_3MgSiO_{12}$: xNi^{2+} (*x* = 1%-10%) phosphors.

x (mol%)	Lifetime τ_1 (μs)	Lifetime τ_2 (μs)	A_1	A_2	χ^2	Lifetime τ^* (μs)
1%	131.77	555.51	880.48	1189.25	1.006	492.21
3%	115.09	393.73	1269.30	1131.06	0.978	324.90
5%	77.61	276.81	1509.88	1238.86	0.941	226.08
7%	65.12	224.01	1524.95	1040.09	0.999	176.53
10%	60.91	186.60	1921.94	875.30	0.958	134.12

2.2.2. Cr^{3+}/Ni^{2+} Co-Doped $Y_3Al_3MgSiO_{12}$

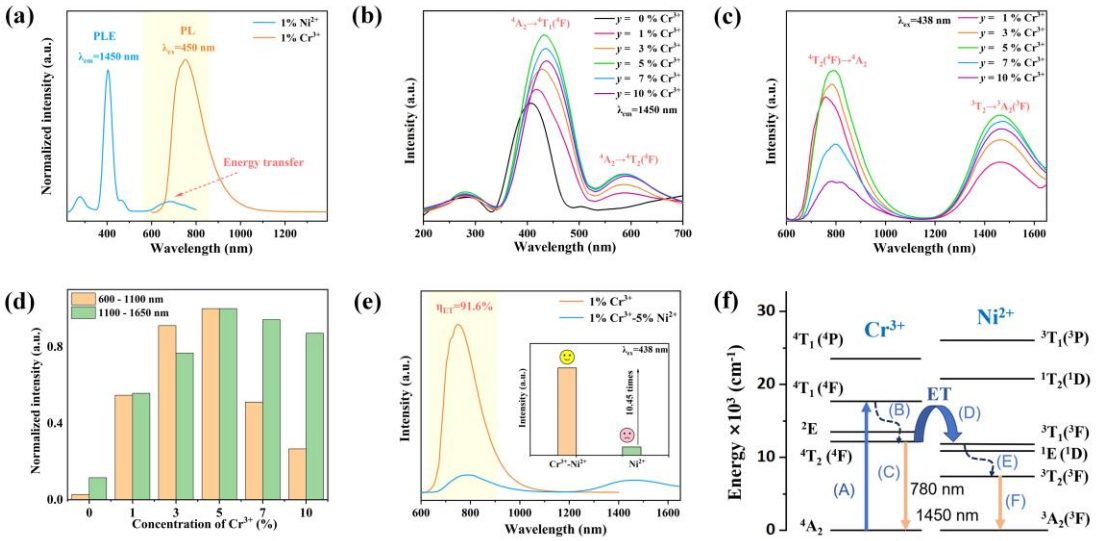


Fig. 6. (a) Emission spectra of $Y_3Al_3MgSiO_{12}$: 1% Cr^{3+} and excitation spectra of $Y_3Al_3MgSiO_{12}$: 1% Ni^{2+}. (b-c) Excitation and emission spectra of $Y_3Al_3MgSiO_{12}$: 5% Ni^{2+}-$y$$Cr^{3+}$ (y = 1% - 10%) phosphors. (d) Dependence of integrated emission intensity in 600-1100 nm and 1100-1650 nm spectral ranges on Cr^{3+} concentration. (e) The energy transfer efficiency of $Y_3Al_3MgSiO_{12}$: 5% Ni^{2+}-1% Cr^{3+}. The inset shows the SWIR intensity of $Y_3Al_3MgSiO_{12}$: 5% Ni^{2+}, $Y_3Al_3MgSiO_{12}$ 5% Cr^{3+}-5% Ni^{2+}. (f) Energy transfer (ET) process diagram of Cr^{3+} and Ni^{2+} in $Y_3Al_3MgSiO_{12}$.

Although the Ni^{2+} doped $Y_3Al_3MgSiO_{12}$ phosphor can be excited by 408 nm light and exhibit broadband SWIR luminescence, its excitation efficiency for commercial blue LED chips is still not efficient enough, and the luminescence performance can be further improved. Therefore, we introduce the co-doping of Cr^{3+} and Ni^{2+} to act as sensitizers to adjust the excitation band and improve the luminescence properties of the phosphors. As shown in Fig. 6(a), compared with $Y_3Al_3MgSiO_{12}$: Ni^{2+}, the excitation band of $Y_3Al_3MgSiO_{12}$: Cr^{3+} is dominant in the blue region. A clear overlap is observed between the emission spectrum of $Y_3Al_3MgSiO_{12}$: 1% Cr^{3+} and the excitation spectrum of $Y_3Al_3MgSiO_{12}$: 1% Ni^{2+} within the 600-850 nm wavelength range. This indicates that there is an energy transfer phenomenon between Cr^{3+} and Ni^{2+} ions [42].

Fig. 6(b) shows the excitation spectra of $Y_3Al_3MgSiO_{12}$: 5% Ni^{2+}-$y$$Cr^{3+}$($y$ = 1%-10%) phosphors monitored at 1450 nm. With the gradual increase of Cr^{3+} concentration, the excitation band intensities of $^3A_2$ (^3F)→$^3T_1$ (^3P) and $^3A_2$ (^3F)→$^3T_1$ (^3F) transitions of Ni^{2+} ions gradually decrease. At the same time, the excitation bands of $^4A_2$ (^4F)→$^4T_1$ (^4F) and $^4A_2$ (^4F)→$^4T_2$ (^4F) transitions of Cr^{3+} ions gradually dominate the spectrum, which corresponds to the distribution of $Y_3Al_3MgSiO_{12}$: 5% Ni^{2+}-5%Cr^{3+} absorption bands in DR spectrum (Fig. 3(a)). The change in the excitation spectrum further supports the occurrence of energy transfer from Cr^{3+} to Ni^{2+}, thereby enabling more efficient excitation of Ni^{2+}-doped phosphors using blue LED chips.

As shown in Fig. 6(c), under the excitation of 438 nm blue light, $Y_3Al_3MgSiO_{12}$: 5% Ni^{2+}-$y$$Cr^{3+}$ (y = 1%-10%) phosphors exhibit two broad emission bands at 600-1100 nm and 1100-1650 nm, which are Cr^{3+} ion emission in the NIR-I region and Cr^{3+} emission and Ni^{2+} emission in the SWIR region, respectively. Compared with the sample without Cr^{3+}, the introduction of Cr^{3+} significantly improves the emission intensity of Ni^{2+} in the SWIR region. This phenomenon is attributed to the energy transfer from Cr^{3+} to Ni^{2+}, which greatly enhances the Ni^{2+} emission with low emission efficiency under blue light excitation [43]. As the Cr^{3+} concentration increases, the integrated emission intensity in the 600-1650 nm regions and only in the 1100-1650 nm region showed a trend of increasing first and then decreasing. Among them, $Y_3Al_3MgSiO_{12}$: 5% Cr^{3+}-5% Ni^{2+} has the highest luminous intensity, as shown in Fig. 6(d). The emission intensity of $Y_3Al_3MgSiO_{12}$: 5% Cr^{3+}-5% Ni^{2+} sample is 10.45 times higher than that of

$Y_3Al_3MgSiO_{12}$: 5% Ni^{2+} sample monitored at 438 nm. In the process of energy transfer, the resonance ET from sensitizer to activator is mainly realized by two interaction modes: exchange interaction and multipole interaction. According to G. Blasse 's theory, R_c between the sensitizer (Cr^{3+}) and the activator (Ni^{2+}) is a key parameter to determine the dominant energy transfer mechanism in $Y_3Al_3MgSiO_{12}$: Ni^{2+}-Cr^{3+} phosphors. When R_c is less than 0.5 nm, the exchange interaction becomes the main mode. When R_c is greater than 0.5 nm, the energy transfer process mainly depends on the multipole interaction [44-45]. The specific value of R_c can be calculated by Eq. (6). In $Y_3Al_3MgSiO_{12}$: 5% Ni^{2+}-5% Cr^{3+} phosphor, the total concentration x_c of dopants (Cr^{3+} and Ni^{2+}) is 0.1, the unit cell volume V is 1731.242 $Å^3$. According to these parameters, the R_c between the sensitizer (Cr^{3+}) and the activator (Ni^{2+}) is calculated to be 1.61 nm, which is significantly greater than 0.5 nm. This result shows that the energy transfer from Cr^{3+} to Ni^{2+} mainly depends on the multipole interaction.

Fig. 6(e) compares the emission intensities of $Y_3Al_3MgSiO_{12}$: 1% Cr^{3+} and $Y_3Al_3MgSiO_{12}$: 5% Ni^{2+}-1% Cr^{3+}. The emission intensity of Cr^{3+} in the NIR-I region diminished following the incorporation of Ni^{2+}, whereas the emission intensity of Ni^{2+} in the SWIR region augmented. This substantiates the hypothesis that Cr^{3+} ions transfer energy to Ni^{2+}. The energy transfer efficiency can be calculated using the following formula [46]:

$$\eta = 1 - \frac{I_1}{I_2} \quad (12)$$

Among them, η is the energy transfer efficiency of Cr^{3+} ions to Ni^{2+} ions, I_1 and I_2 represent the PL intensity of Cr^{3+} in the Ni^{2+}-doped and Ni^{2+}-free phosphors. The calculated η value is 91.6%, indicating that $Y_3Al_3MgSiO_{12}$: Ni^{2+}- Cr^{3+} has an excellent energy transfer efficiency. The energy level diagram of $Y_3Al_3MgSiO_{12}$: Ni^{2+}- Cr^{3+} (Fig. 6(f)) provides a clear explanation of the energy transfer mechanism between Cr^{3+} and Ni^{2+}. Upon excitation by 438 nm blue light, electrons initially at the $^4A_2$ ground state of Cr^{3+} are promoted to the $^4T_1$ (F) energy level, then undergo non-radiative relaxation down to the $^4T_2$ (F) level. Some electrons then return to the $^4A_2$ ground state *via* radiative transitions, resulting in 780 nm Cr^{3+} emission, while part of the energy is transferred to the nearby Ni^{2+} ions, exciting them to the $^3T_1$ (F) level. The excited electrons then undergo non-radiative relaxation to the $^3T_2$ (F) level and eventually return to the $^3A_2$ (F) ground state, producing 1450 nm Ni^{2+} emission. After excitation, the electrons relax non-radiatively to the $^3T_2$ (F) level and eventually return to the $^3A_2$ (F) ground state, producing 1450 nm Ni^{2+} emission. This energy transfer from Cr^{3+} to Ni^{2+} significantly enhances the emission intensity of Ni^{2+} under blue light excitation [47].

The internal quantum efficiency (IQE) of $Y_3Al_3MgSiO_{12}$: 5% Ni^{2+}- 5% Cr^{3+} phosphor was measured at room temperature under 438 nm excitation using an integrating sphere. IQE is defined as the ratio of the number of emitted photons to the number of absorbed photons, as illustrated in Fig. S2. The calculation formula is given as follows:

$$\mathrm{IQE} = \frac{\int L_S}{\int E_R - \int E_S} \quad (13)$$

Here, L_S represents the number of photons emitted by the sample, while E_R and E_S denote the number of reflected excitation photons from the $BaSO_4$ reference and the sample, respectively. Under 438 nm excitation and within the detection range of 200-1650 nm, the IQE of the sample was measured to be 16.8%. The external quantum efficiency (EQE) is defined as the ratio of the number of emitted photons to the number of incident excitation photons, while the absorption efficiency (AE) is the ratio of the number of absorbed photons to the number of incident excitation photons. Accordingly, EQE can be calculated using the following equation [48]:

$$\mathrm{EQE} = \frac{\int L_S}{\int E_R} \quad (14)$$

$$\mathrm{AE} = \frac{\int E_R - \int E_S}{\int E_R} \quad (15)$$

$$\mathrm{EQE} = \mathrm{IQE} \times \mathrm{AE} \quad (16)$$

The experimentally measured AE was 41.6%, based on which the EQE of the sample was calculated to be 6.99% within the 200-1650 nm wavelength range. Fig. S3(a) shows the attenuation curve of near-infrared light emitted by $Y_3Al_3MgSiO_{12}$: 5% Ni^{2+}-$y$$Cr^{3+}$ (y = 1%-10%) phosphors near 1450 nm under 438 nm laser excitation. The average lifetimes calculated by Eq. (9) and Eq. (10) are 285.01 μs, 271.95 μs, 253.76 μs, 242.55 μs and 218.13 μs, respectively. The detailed data of the fitting results are shown in Table S3. Fig. S4(b) reveals the relationship between fluorescence lifetime and y doping content.

2.2.3. Luminous Thermal Stability

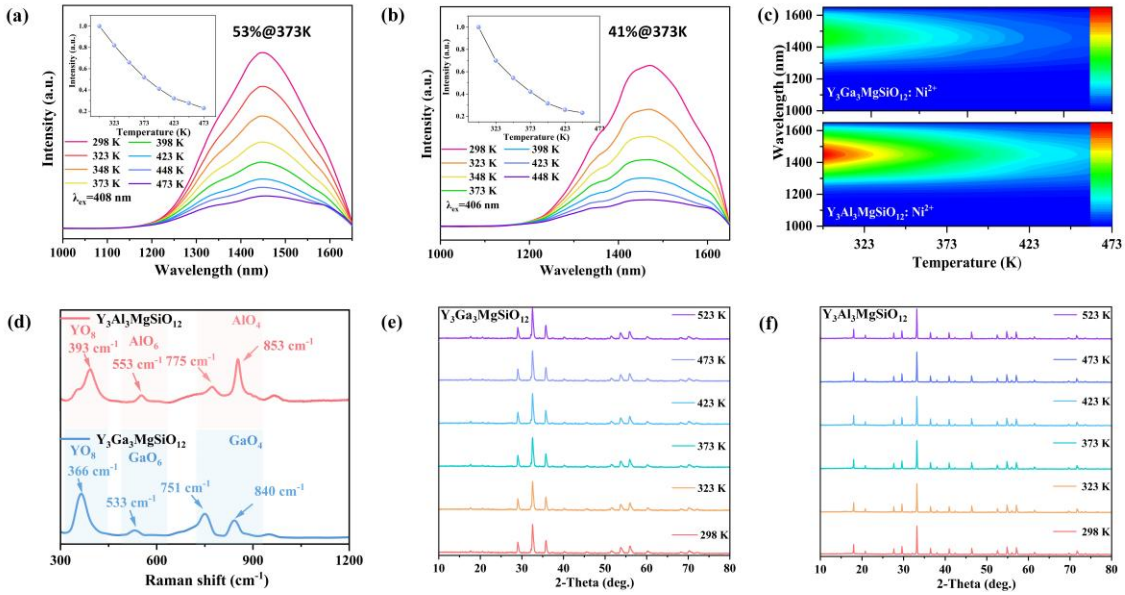


Fig. 7. (a-b) Emission spectra of $Y_3Al_3MgSiO_{12}$: 5% Ni^{2+} and $Y_3Ga_3MgSiO_{12}$: 3% Ni^{2+} phosphor at different temperatures. The inset shows the dependence of integrated emission intensity on temperature. (c) The 2D color plot of SWIR emission as a function of temperature. (d) Raman spectra of $Y_3Ga_3MgSiO_{12}$: Ni^{2+} and $Y_3Al_3MgSiO_{12}$: Ni^{2+}. (e-f) The in situ XRD patterns in the temperature range of 298-523 K.

Fig. 7(a-b) illustrates the temperature-dependent luminescence spectra of $Y_3Al_3MgSiO_{12}$: 5% Ni^{2+} and $Y_3Ga_3MgSiO_{12}$: 3% Ni^{2+}. As the temperature rises, the luminescence intensity declines gradually, while the morphology and peak position of the luminescence spectrum remain largely unaltered. The primary reason for this phenomenon is that at room temperature, the majority of electrons return to the ground state *via* the radiation process. With the increase in temperature, the coupling between electron and phonon is enhanced, which makes it more likely for electrons to return from the excited state to the ground state in a non-radiative manner, resulting in a decrease in luminescence intensity [49]. Fig. 7(c) shows the thermal stability of NIR-II-III emission for $Y_3Ga_3MgSiO_{12}$: 3% Ni^{2+} and $Y_3Al_3MgSiO_{12}$: 5% Ni^{2+} at 373 K, respectively, with the corresponding emission intensities retaining 41% and 53% of their values at room temperature. It is evident from the results that the latter exhibits significantly superior thermal stability, which is attributed to the enhanced rigidity of the crystal structure resulting from the substitution of Ga by Al. The rigidity of the host lattice is a critical

factor in determining the thermal stability of the material, as a robust framework can effectively suppress lattice vibrations and energy dissipation induced by thermal excitation [23]. A comparison of bond lengths reveals that the average Al_1/Mg-O bond length in $Y_3Al_3MgSiO_{12}$ is 1.869 Å, which is markedly shorter than the Ga_1/Mg-O bond length of 2.016 Å in $Y_3Ga_3MgSiO_{12}$, indicating a higher structural rigidity in the former.

To analyze the structural changes induced by the substitution of Ga^{3+} with Al^{3+}, the Raman spectra of $Y_3Ga_3MgSiO_{12}$: 3% Ni^{2+} and $Y_3Al_3MgSiO_{12}$: 5% Ni^{2+} were compared, as shown in Fig. 7(d). In a manner similar to other garnet-type phosphors, the Raman peaks located at 366 and 533 cm^{-1} correspond to the internal vibrational modes of the [YO_8] dodecahedra and [GaO_6] octahedra, respectively, while the peak at 751 and 840 cm^{-1} is assigned to the internal vibrational mode of the [GaO_4] tetrahedra, respectively [50]. Upon substitution of Ga^{3+} by Al^{3+}, the original Raman peaks shift to 393, 553, 775 and 853 cm^{-1}, corresponding to the characteristic vibrations of [YO_8] dodecahedra, [AlO_6] octahedra and [AlO_4] tetrahedra, respectively. In addition, the original broad peaks in the octahedral and tetrahedral regions became sharper after substitution, indicating a transition from structural disorder to order [9]. This enhancement in structural ordering is attributed to the stronger Al-O bonding compared to Ga-O [51].

To further evaluate the influence of Al substitution on lattice rigidity, the Debye temperature ($\Theta_{D,i}$) was estimated using the following equation based on the isotropic atomic displacement parameter ($U_{iso,i}$):

$$\Theta_{D,i} = \sqrt{\frac{3\hbar T N_A}{A_i k_B U_{iso,i}}} \quad (17)$$

Here, $\hbar$ is Planck's constant, A_i is the atomic mass, k_B is Boltzmann's constant, and $U_{iso,i}$ is the atomic displacement parameter of the corresponding atom. The value of $\Theta_{D,i}$ is inversely proportional to $U_{iso,i}$. According to the Rietveld refinement results shown in Fig. S4, the Al_1 site of $Y_3Al_3MgSiO_{12}$: 5% Ni^{2+} exhibits lower $U_{iso,i}$ ($U_{iso,i}$ = 0.0165) values compared to the Ga_1 site of $Y_3Ga_3MgSiO_{12}$: 3% Ni^{2+} ($U_{iso,i}$ = 0.0264). In addition, based on the DFT-PBE elastic constant calculations, the Debye temperatures of $Y_3Ga_3MgSiO_{12}$

and $Y_3Al_3MgSiO_{12}$ were determined to be 649 K and 725 K, respectively, which is consistent with the experimental trend [27, 52]. These results confirm a positive correlation between Debye temperature and lattice rigidity, further demonstrating that Al substitution enhances the lattice stiffness [48].

Fig. 7(e-f) presents the *in situ* XRD results of $Y_3Ga_3MgSiO_{12}$: 3% Ni^{2+} and $Y_3Al_3MgSiO_{12}$: 5% Ni^{2+} samples within the range of 298-573 K. With increasing temperature, no significant changes in diffraction peak shapes were observed, indicating that both phosphors exhibit good thermal stability. To further clarify the phase information at different temperatures, Rietveld refinements of the variable-temperature XRD data were performed in Fig. S5-S6, and the corresponding results are summarized in Table S4-S7. All parameters met the reliability criteria, and the diffraction data of the samples at different temperatures were well fitted. The variation of unit-cell volume (V) with temperature, as obtained from refinement, is shown in Fig. S7. The results reveal that the unit-cell volumes of $Y_3Ga_3MgSiO_{12}$: 3% Ni^{2+} and $Y_3Al_3MgSiO_{12}$: 5% Ni^{2+} both expand with increasing temperature. The thermal expansion coefficient (α) can be calculated using the following equation [53]:

$$\alpha = \frac{1}{V_0} \times \frac{\Delta V}{\Delta T} \quad (18)$$

Here, V_0 represents the material volume at the initial temperature, ΔV denotes the corresponding volume change, and ΔT is the temperature variation. The calculated thermal expansion coefficients are α_1 = 9.287 × 10^{-6} K^{-1} and α_2 = 4.559 × 10^{-6} K^{-1}, respectively. The lower thermal expansion coefficient further indicates that lattice rigidity is enhanced when Al substitutes Ga, thereby providing a structural basis for the superior thermal quenching resistance of $Y_3Al_3MgSiO_{12}$: Cr^{3+}-Ni^{2+} at elevated temperatures [54].

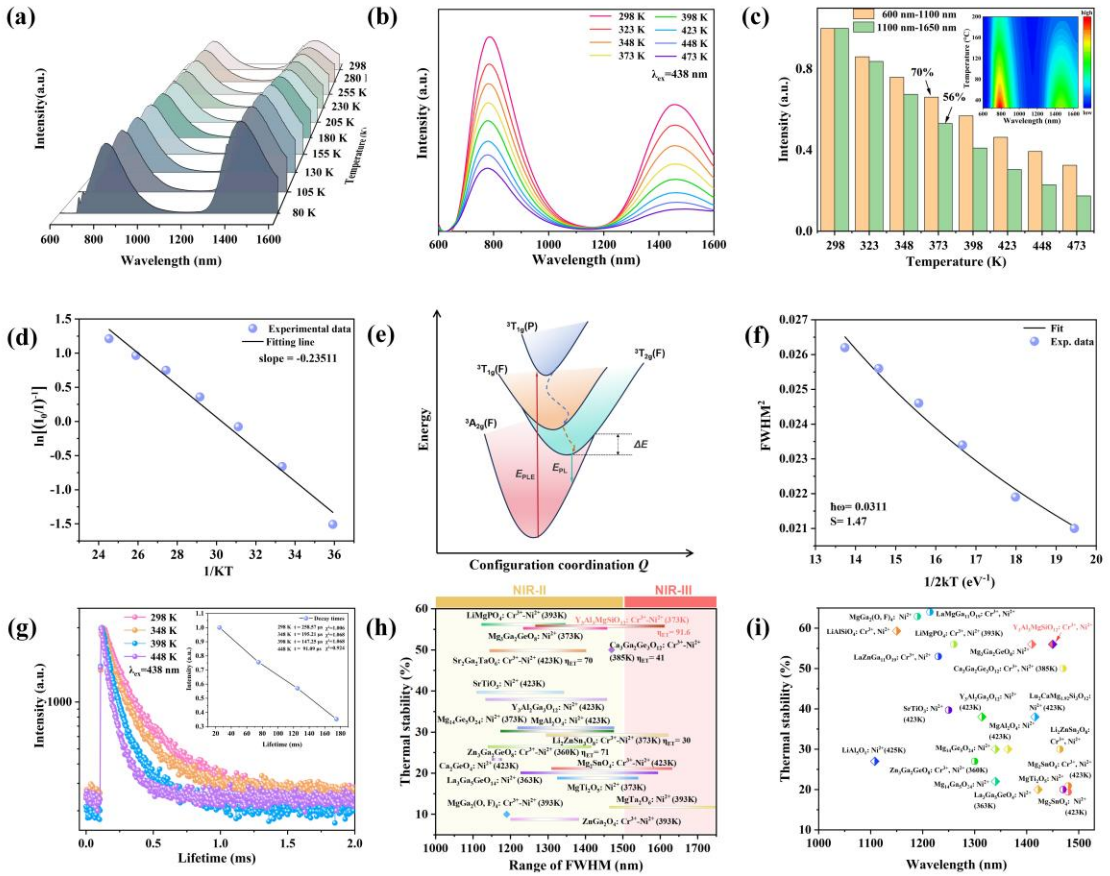


Fig. 8. (a-b) Emission spectra of $Y_3Al_3MgSiO_{12}$: 5% Ni^{2+}-5% Cr^{3+} phosphor at different temperatures. (c) Dependence of integrated emission intensity in the wavelength range of 600-1100 nm and 1100-1650 nm on temperature. The inset shows the 2D color plot of SWIR emission as a function of temperature. (d) The plot of $\ln(I_0/I_T)^{-1}$ *versus* $1/kT$ of the phosphor. (e) Configurational coordinate diagram of Ni^{2+}. (f) $FWHM^2$ *versus* $1/2kT$ plot. (g) The decay curves of $Y_3Al_3MgSiO_{12}$: 5% Ni^{2+}-5% Cr^{3+} for 1450 nm emission at different temperatures. The inset shows the temperature-dependent fluorescence lifetime. (h) Survey of emission wavelength, thermal stability, FWHM, and energy transfer efficiency of Ni^{2+} and Cr^{3+}-Ni^{2+} activated SWIR phosphors. (i) Comparison of thermal stability for Ni^{2+} and Cr^{3+}-Ni^{2+} SWIR phosphors across different emission positions.

Fig. 8(a) presents the emission spectra of $Y_3Al_3MgSiO_{12}$: 5% Ni^{2+}-5% Cr^{3+} phosphor recorded from 80 K to room temperature. As the temperature increase, the emission bands become progressively broader, primarily due to the enhanced electron-phonon interactions [26]. The vibrational amplitude of luminescent ions around their equilibrium positions in the host lattice increases with heating, thereby broadening the energy

distribution of the $^4T_2 \rightarrow {}^4A_2$ transition of Cr^{3+} in the 600-1100 nm region and the $^3T_2 \rightarrow {}^3A_2$ transition of Ni^{2+} in the 1100-1650 nm region, which leads to an increased bandwidth of the near-infrared emission [47].

In Fig. 8(b-c), the emission spectra of $Y_3Al_3MgSiO_{12}$: 5% Ni^{2+}-5% Cr^{3+} phosphor from room temperature to 473 K indicate that Cr^{3+} ions exhibit better thermal stability compared to Ni^{2+} ions. At 373 K, the phosphor retains 70% and 56% of its room-temperature emission intensity in the NIR-I and NIR-II/III regions, respectively. This is because Ni^{2+} ions typically exhibit a larger Stokes shift than Cr^{3+} ions, resulting in a smaller energy gap between the excited and ground states, which increases the probability of non-radiative processes. As a result, Ni^{2+} ions are more susceptible to thermal quenching at elevated temperatures, whereas Cr^{3+} ions demonstrate superior thermal stability in comparison [55-56]. The activation energy (ΔE) of Ni^{2+}, as illustrated in Fig. 8(d), is determined through the application of the following formula [57]:

$$I_T = \frac{I_0}{1+A\times e^{-\Delta E/kT}} \quad (19)$$

k is the Boltzmann constant, and A is a constant value, I_T indicates that the specific temperature is the integral strength of Ni^{2+}, and I_0 is the emission intensity at the initial temperature. By estimating the slope of the linear fitting curve, the thermal activation energy is 0.23511 eV. Fig. 8(e) shows the schematic diagram of the SWIR spectral deformation of Ni^{2+} caused by thermal quenching. When the excitation is 438 nm, the electron transitions from the $^3A_{2g}$ (F) ground state to the $^3T_{1g}$ (P) excited state. In this process, the near-infrared emission of Ni^{2+} is accompanied by the transfer of electrons from the $^3T_{1g}$ (P) excited state to $^3T_{2g}$ (F) and then returns to the ground state $^3A_{2g}$ (F) through non-radiative relaxation. As the temperature increases, the electron vibration of

the excited state of $^3T_{2g}$ (F) increases, thereby increasing the probability of Ni^{2+} electrons returning to the ground state or high energy state after excitation, which leads to the expansion of the spectral range [47].

The Huang-Kun factor (S) and the average phonon energy ($\hbar\omega$) are key parameters for characterizing the electron-phonon coupling (EPC) strength in $Y_3Al_3MgSiO_{12}$: 5% Ni^{2+}-5% Cr^{3+} phosphors [56]. By fitting the temperature dependence of the FWHM of the SWIR emission spectrum, their values can be determined by the following equation:

$$FWHM = 2.36\sqrt{S}\,\hbar\omega\sqrt{\coth\left(\frac{\hbar\omega}{2kT}\right)} \quad (20)$$

Here, k is the Boltzmann constant. As shown in Fig. 8(f), by fitting the $FWHM^2$ with $1/(2kT)$, S = 1.50 and $\hbar\omega$ = 0.035 eV were obtained. The relatively low value of S suggests that there is weak electron-phonon coupling in the system, which can effectively suppress the probability of non-radiative transitions as the temperature increases [58]. Fig. 8(g) and Fig. S8(a-b) respectively present the temperature-dependent luminescence decay curves at 1450 nm for $Y_3Al_3MgSiO_{12}$: 5% Ni^{2+} and $Y_3Al_3MgSiO_{12}$: 5% Ni^{2+}-5% Cr^{3+} phosphors under 408 nm and 438 nm excitation. The decay profiles were well-fitted using a double-exponential decay model (Eq. (8)), and the average lifetimes were calculated using Eq. (9) [59]. Detailed fitting parameters are listed in Table S8 and Table S9. With increasing temperature, the fluorescence lifetime of the phosphor gradually decreases, which is primarily attributed to thermal quenching resulting from enhanced non-radiative relaxation processes. Under thermal excitation, intensified lattice vibrations increase the rate of non-radiative transitions, thereby significantly reducing the fluorescence lifetime. The non-radiative transition rate p can be estimated using the

following equation [24,59]:

$$\tau_T = \frac{1}{\frac{1}{\tau_0}+pexp(-\frac{\Delta E}{kT})} \quad (21)$$

Here, τ_0 and τ_T represent the fluorescence lifetimes at room temperature and a given elevated temperature, respectively. ΔE can be obtained by fitting the experimental data using the Arrhenius equation, and was calculated to be 0.23511 eV in Eq. (19). Since the non-radiative transition rate increases positively with temperature, the observed decrease in fluorescence lifetime can be reasonably explained.

Fig. 8(h) summarizes the luminescence performance parameters of Ni^{2+} singly doped and Cr^{3+}-Ni^{2+} co-doped SWIR phosphors reported in the previous studies, including emission position, FWHM, energy transfer efficiency, and thermal stability. Fig. 8(i) compares the thermal stability (373 K) at different emission positions. In general, the emission bands of most previously reported Ni^{2+}/Cr^{3+}-Ni^{2+} doped materials are primarily concentrated in the NIR-II region, making it difficult to achieve coverage in the longer-wavelength NIR-III region. Moreover, their relatively low energy transfer efficiency and limited thermal stability restrict their potential for applications in the SWIR region. In the NIR-II/III region, especially NIR-III emission, it exhibits strong electron-phonon coupling and poor thermal stability. In contrast, the $Y_3Al_3MgSiO_{12}$: Cr^{3+}-Ni^{2+} phosphor synthesized in this work can achieve ultra-broadband emission spanning the NIR I-III regions under blue-light excitation, with a combined FWHM of up to 496 (185+311) nm. Simultaneously, this material exhibits outstanding energy transfer efficiency and favorable thermal stability, surpassing those of previously reported systems and demonstrating great potential for use in high-performance SWIR light sources.

2.4 Performance of the SWIR pc-LED

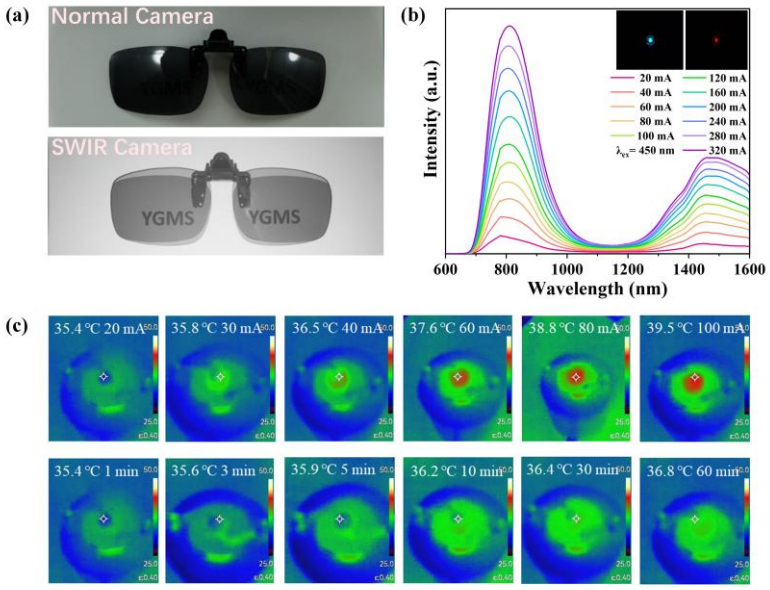


Fig. 9. (a) The visible light images were captured by a standard digital camera under white LED illumination, and the SWIR images were captured by an InGaAs SWIR camera under SWIR pc-LED illumination. (b) PL spectra of SWIR pc-LED under 20 to 320 mA drive currents. (c) SWIR pc-LED under 20-100 mA drive currents and 20 mA drive currents from 1 to 60 minutes, as observed by a thermal imager.

The SWIR pc-LED device was successfully fabricated by integrating the ultra-broadband NIR-emitting $Y_3Al_3MgSiO_{12}$: 5% Ni^{2+}-5% Cr^{3+} phosphor with a commercial 450 nm blue LED chip. Due to the strong penetration capability of SWIR light, the emission from the LED prototype can pass through various materials and enable clear imaging when captured by a SWIR camera. Fig. 9(a) shows the word "YGMS" obscured by a dark filter, making it almost indistinguishable under normal indoor lighting. However, when SWIR LEDs are used in conjunction with commercial SWIR cameras, this information becomes visible, showing the potential of SWIR technology in hidden information detection. Fig. 9(b) shows the relationship between the electroluminescence (EL) spectrum of the device with the driving current (I), respectively. It can be seen that as the driving current increases from 20 mA to 320 mA, the emission intensity of Cr^{3+} in

the NIR-I region and Ni^{2+} in the NIR-II-III region increases with the increase of the driving current.

Fig. 9(c) shows the temperature variation of SWIR LED devices at different input currents and for different durations under the same current condition. As the driving current increases from 20 mA to over 100 mA, the device temperature rises by only 4.1 °C (from 35.4 °C to 39.5 °C). In addition, under continuous operation at 20 mA from 1 to 60 minutes, the device exhibited only a minor temperature rise, from 35.4 °C to 36.8 °C, indicating excellent long-term thermal stability. This suggests that the synthesized $Y_3Al_3MgSiO_{12}$: Cr^{3+}-Ni^{2+} phosphor as a luminescence conversion material is capable of efficiently converting blue light into SWIR radiation, giving it the potential to be used in specific technological applications, especially in areas where thermal stability is required.

2.5. Application in chemical compound identification

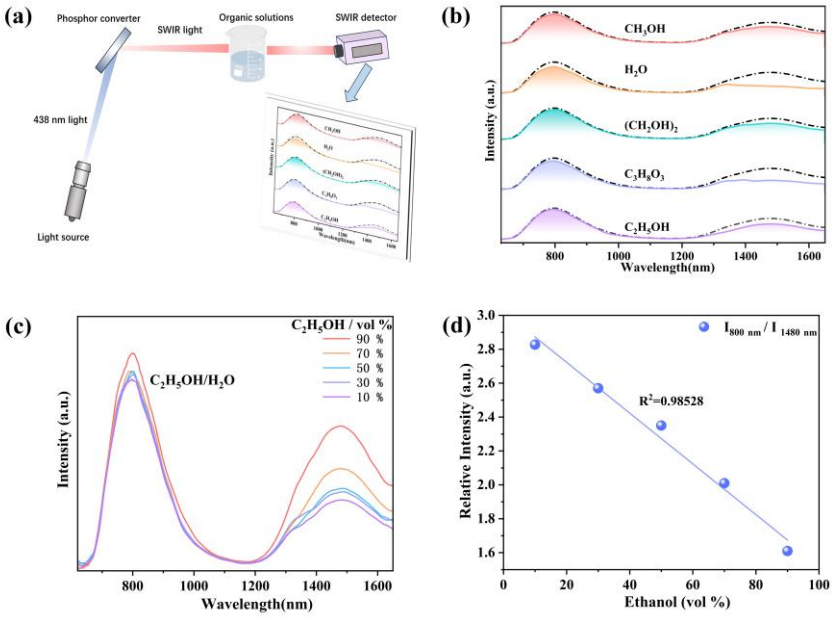


Fig. 10. (a) Schematic diagram of the SWIR spectroscopy analytical device. (b) The original spectrum of $Y_3Al_3MgSiO_{12}$: 5%Cr^{3+}-5%Ni^{2+} (dashed line) and the spectra after penetrating different solvents. (c) Spectra of SWIR light from the phosphor after

penetrating C_2H_5OH/H_2O solution with different C_2H_5OH concentration. (d) Relationships between the relative PL intensity ratio of band 800 to 1480 nm with the C_2H_5OH concentration in C_2H_5OH/H_2O solution.

Due to the specific scattering and absorption characteristics of different substances in SWIR region, particularly the overtone and vibrational absorption of O-H and C-H bonds within the NIR-II-III range [16,18]. These features can be clearly observed in the transmission spectra. The $Y_3Al_3MgSiO_{12}$: Cr^{3+}-Ni^{2+} phosphor exhibits stable emission in the NIR-I region (700-1000 nm) and high sensitivity to vibrational absorption in the NIR-II–III region (1000-1700 nm), thereby providing a solid spectral foundation for both qualitative and quantitative analysis of organic solvents. To evaluate the potential of this phosphor in nondestructive testing, a SWIR spectral analysis setup was constructed, as shown in Fig. 10(a). The setup comprises a phosphor-based light source excited by a xenon lamp (λ_{ex}= 438 nm) and an NIR detector. Various organic solvents were placed between the phosphor light source and the detector. As illustrated in Fig. 10(b), by comparing the original PL spectrum of the phosphor with its SWIR emission spectra after transmission through different solvents, distinct solvent-specific absorption bands were observed: H_2O (~1340 nm), CH_3OH (~1460 nm), C_2H_5OH (~1480 nm), $(CH_2OH)_2$ (~1400 and 1505 nm), and $C_3H_8O_3$ (~1345 and 1390 nm). These differences clearly demonstrate the phosphor's capability to distinguish between different solvents. As shown in Fig. 10(c), based on the varying absorption intensities of C_2H_5OH in the NIR-I and NIR-II–III regions, the intensity ratio (I_{800nm}/I_{1480nm}) was employed to quantitatively detect the ethanol concentration in C_2H_5OH/H_2O mixtures. As the C_2H_5OH concentration increased from 10 to 90 vol%, the absorption intensities at 800 nm and 1480 nm varied accordingly, and the intensity ratio exhibited a strong linear correlation with

concentration, R^2 = 0.98528 (Fig. 10(d)). These results verify the excellent ethanol recognition capability of the SWIR emission from $Y_3Al_3MgSiO_{12}$: Cr^{3+}-Ni^{2+}, further highlighting the potential of SWIR spectroscopy for quantitative analysis of organic compounds. Owing to its stable near-infrared emission and good compatibility with NIR detectors, this phosphor exhibits promising potential for practical applications in non-contact, nondestructive detection scenarios.

Conclusion

In this study, a series of $Y_3Al_3MgSiO_{12}$: Ni^{2+} and $Y_3Al_3MgSiO_{12}$: Cr^{3+}-Ni^{2+} SWIR phosphors were synthesized *via* a conventional solid-state reaction method. The $Y_3Al_3MgSiO_{12}$: Ni^{2+} phosphor exhibited ultra-broadband SWIR emission covering the range of 1100-1650 nm under 408 nm excitation. Compared to the Ni^{2+} doped sample, the co-doped phosphor exhibited a 10.45-fold increase in emission intensity and maintained 56% of its NIR-II-III emission intensity at 373 K relative to room temperature, demonstrating excellent thermal stability. This can be attributed to the increased crystal structure rigidity following Ga/Al substitution and the smaller Huang-Rhys factor, which allows for weaker electron-phonon coupling. Compared to other Cr^{3+}-Ni^{2+} co-doped phosphors reported in the literature, this work achieves efficient energy transfer from Cr^{3+} to Ni^{2+}, with an energy transfer efficiency (η) of up to 91.6%, significantly enhancing the blue light absorption intensity. The Cr^{3+}-Ni^{2+} co-doped $Y_3Al_3MgSiO_{12}$ phosphor displayed ultra-broadband emission spanning 600-1650 nm under 438 nm excitation, with a FWHM of (185+311) nm. Furthermore, a SWIR phosphor-converted LED (pc-LED) device was successfully fabricated by integrating the phosphor with a 450 nm blue LED chip, confirming its potential for SWIR applications such as covert information

recognition and non-contact, nondestructive detection scenarios. This work not only introduces a high-performance ultra-broadband SWIR phosphor but also provides valuable guidance for the rational design of efficient Cr^{3+}/Ni^{2+} co-doped SWIR materials excitable by blue light.

CRediT authorship contribution statement

Qian Zhang: Investigation, Data curation, Writing-original draft. Xinyu Li: Methodology. Ziying Wang: Data curation. Qi Zhu: Resources. Xuejiao Wang: Funding acquisition, Supervision. Jiguang Li: Writing-review&editing.

Declaration of competing interest

The authors of the study report no conflicting interests.

Data availability

Data will be made available on request.

Acknowledgements

This work is supported by the Liaoning Revitalization Talents Program (Grant No. XLYC2403017), the Natural Science Foundation of the Education Department of Liaoning Province (Grant No. JYTMS20231627), and the Young Talents Program of Jinzhou (Grant No. JXYC230103). The authors would also like to acknowledge the support from Scientific Compass (www.shiyanjia.com).

References

[1] R.J. Xie, Light-emitting diodes: brighter NIR-emitting phosphor making light sources smarter, *Light: Sci. Appl*., 2020, **9**, 1.

[2] Z. Hu, C. Fang, B. Li, Z. Zhang, C. Cao, M. Cai, S. Su, X. Sun, X. Shi, C. Li, T. Zhou, Y. Zhang, C. Chi, P. He, X. Xia, Y. Chen, S. S. Gambhir and Z. Cheng, First-in-human liver-tumour surgery guided by multispectral fluorescence imaging in the visible and near-infrared-I/II windows, *Nat. Biomed. Eng.,* 2019, **4**, 259-271.

[3] F. Zhu, Y. Gao, B. Zhu, L. Huang and J. Qiu, Ni^{2+}-doped $MgTa_2O_6$ phosphors capable of near-infrared II and III emission under blue-light excitation, *Chem. Eng. J.*, 2024, **479**, 147568.

[4] J. Huang and K. Pu, Activatable Molecular Probes for Second Near-Infrared Fluorescence, Chemiluminescence, and Photoacoustic Imaging, *Angew. Chem. Int. Ed*., 2020, **59**, 11717-11731.

[5] S. Diao, G. Hong, A.L. Antaris, J.L. Blackburn, K. Cheng, Z. Cheng and H. Dai, Biological imaging without autofluorescence in the second near-infrared region, *Nano Res.*, 2015, **8**, 3027-3034.

[6] C. Li, G. Chen, Y. Zhang, F. Wu and Q. Wang, Advanced Fluorescence Imaging Technology in the Near-Infrared-II Window for Biomedical Applications, *J. Am. Chem. Soc.*, 2020, **142**, 14789-14804.

[7] V. Rajendran, H. Chang, R. Liu and R.S. Liu, Recent progress on broadband near-infrared phosphors-converted light emitting diodes for future miniature spectrometers, *Opt. Mater.*, 2019, **1**, 100011.

[8] H. Chang, F.Q. He, E.H. Songa and Q.Y. Zhang, Site-selective occupancy of Cr^{3+} enabling tunable emission from near-infrared I to II in fluoride $LiInF_4:Cr^{3+}$, *J. Mater. Chem. C.*, 2024, **12**, 3175-3184.

[9] L. Yan, G. Zhu, S. Ma, S. Li, Z. Li, X. Luo and B. Dong, Emerging Fe^{3+} Doped Broad NIR-Emitting Phosphor $Ca_{2.5}Hf_{2.5}(Ga, Al)_3O_{12}$: Fe^{3+} for LWUV Pumped NIR LED, *Laser & Photonics Rev.*, 2024, **18**, 2301200.

[10] X. Zhu, S. Zhang and S. Ye, Does Mn^{2+}-Mn^{2+} Spin-Exchange Interaction Involve Mn^{2+} Luminescence of Mn^{2+}-Doped/Concentrated Materials, *J. Phys. Chem. Lett.*, 2024**,**

15, 2804-2814.

[11] M.H. Fang, G.N.A. De Guzman, Z. Bao, N. Majewska, S. Mahlik, M. Grinberg, G. Leniec, S.M. Kaczmarek, C.W. Yang, K.M. Lu, H.S. Sheu, S.F. Hu and R.S. Liu, Ultra-high-efficiency near-infrared Ga_2O_3: Cr^{3+} phosphor and controlling of phytochrome, *J. Mater. Chem. C.*, 2020, **8**, 11013-11017.

[12] Y. Zhao, X. Wang, Q. Wang, T. Zhou, Y. Chen, J. Xu, X. Tang and R.J. Xie, Abnormal spectral broadening of ordered-structure near-infrared phosphor La_2CaHfO_6: Cr^{3+}, *J. Mater. Chem. C.*, 2024, **12**, 10532-10539.

[13] H. Cai, H. Chen, H. Zhou, J. Zhao, Z. Song and Q.L. Liu, Controlling Cr^{3+}/Cr^{4+} concentration in single-phase host toward tailored super-broad near-infrared luminescence for multifunctional applications, *Mater. Today Chem*., 2021, **22**, 100555.

[14] M. Jin, F. Li, J. Xia, L. Zhu, Q. Zhu and J.G. Li, A new persistent luminescence phosphor of $ZnGa_2O_4$: Ni^{2+} for the second near-infrared transparency window, *J. Alloys Compd.*, 2023, **931**, 167491.

[15] C.J. Tang, B.M. Liu, L. Huang, J. Wang and Q. Tang, Ni^{2+}-activated $MgTi_2O_5$ with broadband emission beyond 1200 nm for NIR-II light source applications, *J. Mater. Chem. C.*, 2022, **10**, 18234-18240.

[16] C. Wang, J. Lin, X. Zhang, H. Dong, M. Wen, S. Zhao, S. Yuan, D. Zhu, F. Wu and Z. Mu, Efficient ultra-broadband NIR-II emission achieved by multi-site occupancy in $Mg_3Ga_2GeO_8$: Ni^{2+} phosphor, *J. Alloys Compd.*, 2023, **942**, 168893.

[17] L. Yuan, Y. Jin, D. Zhu, Z. Mou, G. Xie and Y. Hu, Ni^{2+}-Doped Yttrium Aluminum Gallium Garnet Phosphors: Bandgap Engineering for Broad-Band Wavelength-Tunable Shortwave-Infrared Long-Persistent Luminescence and Photochromism, *ACS Sustain.*

Chem. Eng., 2020, **8**, 6543-6550.

[18] B.M. Liu, X.X. Guo, L. Huang, R.F. Zhou, R. Zou, C.G. Ma and J. Wang, A Super-Broadband NIR Dual-Emitting Mg_2SnO_4: Cr^{3+}, Ni^{2+} Phosphor for Ratiometric Phosphor-Converted NIR Light Source Applications, *Adv. Mater. Technol.*, 2022, **8**, 2201181.

[19] F. Zhu, Y. Gao, J. Ding and J. Qiu, Synergistic enhancement of the near-infrared luminescence properties of Ni^{2+}-doped $SrTiO_3$ perovskite phosphors and their application, *J. Mater. Chem. C.*, 2023, **11**, 10236-10246.

[20] S. Miao, Y. Liang, R. Shi, W. Wang, Y. Li and X.J. Wang, Broadband Short-Wave Infrared-Emitting $MgGa_2O_4$:Cr^{3+}, Ni^{2+} Phosphor with Near-Unity Internal Quantum Efficiency and High Thermal Stability for Light-Emitting Diode Applications, *ACS Appl. Mater. Interfaces*., 2023, **15**, 32580-32588.

[21] B.M. Liu, X.X. Guo, L.Y. Cao, L. Huang, R. Zou, Z. Zhou and J. Wang, A High-efficiency blue-LED-excitable NIR-II-emitting MgO: Cr^{3+}, Ni^{2+} phosphor for future broadband light source toward multifunctional NIR spectroscopy applications, *Chem. Eng. J.*, 2023, **452**, 139313.

[22] G. Merkininkaite, A. Zabiliūtė-Karaliūnė, T. Jüstel, V. Klimkevicius, S. Sakirzanovas and A. Katelnikovas, $Ce^{3+} \rightarrow Cr^{3+}$ energy transfer in $Y_3Al_3MgSiO_{12}$ garnet host and application in horticultural lighting, *Ceram. Int.*, 2023, **49**, 16796-16808.

[23] Y. Wang, Y. Xu and Z. Shang M, Simultaneous NIR emission and thermal stability enhancement in garnet-type NIR phosphors through the synergistic effect of lattice distortion and enhanced rigidity, *Laser & Photonics Rev.*, 2024, **18**, 2400295.

[24] T. Liu, Z. Liu, J. Wu, K. Zhang, H. An, Z. Hu and H. Li, Broadband near-infrared persistent luminescence in Ni^{2+}-doped transparent glass-ceramic $ZnGa_2O_4$, *New J. Chem.*,

2022, **46**, 851-856.

[25] L. Fang, L. Lu, L. Zhang, H. Wu, G. Pan, Z. Hao and J. Zhang, Ni^{2+} activated broadband near-infrared II germanate phosphor for pc-LED applications, *J. Alloys Compd.*, 2024, **1003**, 175743.

[26] J. Wang, L. Jiang, R. Pang, S. Zhang, D. Li, K. Li, C. Li and H. Zhang, Cr^{3+}-doped borate phosphors for broadband near-infrared LED applications, *Inorg. Chem. Front.*, 2022, **9**, 2240-2251.

[27] Z. Liao, M. Sójka, J. Zhong and J. Brgoch, Developing the $Na_2CaZr_2Ge_3O_{12}$: Cr^{3+} garnet phosphor for advanced NIR pc-LEDs in night vision and bioimaging, *Chem. Mater.*, 2024, **36**, 4654-4663.

[28] J. Wang, L. Jiang, R. Pang, S. Zhang, D. Li, K. Li and H. Zhang, Cr^{3+}-doped borate phosphors for broadband near-infrared LED applications, *Inorg. Chem. Front.*, 2022, **9**, 2240-2251.

[29] Z. Fu, S. Zhou, T. Pan and S. Zhang, Band structure calculations on the monoclinic bulk and nano-$SrAl_2O_4$ crystals, *J. Solid State Chem.*, 2005, **178**, 230-233.

[30] S. Wu, G. Zhou, Y. Wu, P. Xiong, B. Xiao and Z. Zhou, Multiple Defect-Induced High-Resolution Near-Infrared Mechanoluminescent Materials for Non-Destructive Detection of Blood Glucose and Lipids, *Adv. Mater.*, **2024**, 36, 2408508.

[31] C.Y. Chang, M.H. Huang, K.C. Chen, W.T. Huang, M. Kamiński, N. Majewska, T. Klimczuk, J.H. Chen, D.H. Cherng, K.M. Lu, W.K. Pang, V.K. Peterson, S. Mahlik, G. Leniec and R.S. Liu, Ultrahigh Quantum Efficiency Near-Infrared-II Emission Achieved by Cr^{3+} Clusters to Ni^{2+} Energy Transfer, *Chem. Mater.*, 2024, **36**, 3941-3948.

[32] Y. Duan, Y. Liu, G. Zhang, L. Yao and Q. Shao, Broadband Cr^{3+}-sensitized

upconversion luminescence of $LiScSi_2O_6:Cr^{3+}/Er^{3+}$, *J. Rare Earths.*, 2021, **39**, 1181-1186.

[33] Z. Gao, Y. Zhang, Y. Li, S. Zhao, P. Zhang, X. Dong, D. Deng and S. Xu, Blue light-excited broadband NIR-II-emitting $Li_2ZnSn_3O_8$: Cr^{3+}, Ni^{2+} phosphor for multifunctional optical applications, *Inorg. Chem. Front.*, 2024, **11**, 4711-4720.

[34] S. Miao, Y. Liang, Y. Zhang, D. Chen and X.J. Wang, Blue LED-Pumped Broadband Short-Wave Infrared Emitter Based on $LiMgPO_4:Cr^{3+}$, Ni^{2+} Phosphor, *Adv. Mater. Technol.*, 2022, **7**, 2200320.

[35] L. Jiang, L. Zhang, X. Jiang, J. Xie, G. Lv and Y. Su, Cr^{3+}-Yb^{3+}-Ni^{2+} Tri-Doped NIR Phosphors with Spectral Output Covering NIR-I and NIR-II Regions, *Adv. Mater. Technol*., 2024, **9**, 2301495.

[36] F. Zhao, Y. Shao, Q. Liu and J. Zhong, Blue-Light-Excitable Broadband $Ca_3Ga_2Ge_3O_{12}$: Cr^{3+}, Ni^{2+} Phosphor for the Applications in NIR-II Window, *Laser & Photonics Rev.*, 2024, **18**, 2400447.

[37] L. Zheng, H. Wu, K. Zhao, Y. Liu, S. Wen, G.H. Pan, H. Wu, Z. Hao, L. Zhang, and J. Zhang, Ultrabroadband Near-Infrared $Zn_3Ga_2GeO_8$: Cr^{3+}, Ni^{2+} Phosphor for PiG pc-LED, *Adv. Opt. Mater.*, 2024, **12**, 2401521.

[38] J. Wang, C. Gong, S. Yang, Q. Zhu, X. Wang and J.G. Li, Cr^{3+} activated $Na_3RESi_3O_9$ (RE = Y, Lu, Sc) silicate broadband near-infrared phosphors for luminescence towards NIR-II region via a multi-site occupancy strategy, *J. Rare Earths.*, 2024, **42**, 1447-1457.

[39] C. Wang, Y. Zhang, X. Han, D. Hu, D. He, X. Wang and H. Jiao, Energy transfer enhanced broadband near-infrared phosphors: Cr^{3+}/Ni^{2+} activated $ZnGa_2O_4$-Zn_2SnO_4 solid solutions for the second NIR window imaging, *J. Mater. Chem. C.*, 2021, **9**, 4583-4590.

[40] L. Yao, Q. Shao, S. Han, C. Liang, J. He and J. Jiang, Enhancing near-infrared photoluminescence intensity and spectral properties in Yb^{3+} codoped $LiScP_2O_7$: Cr^{3+}, *Chem. Mater.*, 2020, **32**, 2430-2439.

[41] Y. Zhuo, F. Wu, Y. Niu, Y. Wang, Q. Zhang, Y. Teng and Z. Mu, Super broadband emission across NIR-I and NIR-II under blue light excitation of Cr^{3+}, Ni^{2+} Co-Doped Sr_2GaTaO_6 phosphor achieved by two-site occupation and effective energy transfer, *Laser & Photonics Rev.*, 2024, **18**, 2400105.

[42] V. Rajendran, K.C. Chen, W.T. Huang, M. Kamiński, M. Grzegorczyk, S. Mahlik, G. Leniec, K.M. Lu, D.H. Wei, H. Chang and R.S. Liu, Unraveling Luminescent Energy Transfer Pathways: Futuristic Approach of Miniature Shortwave Infrared Light-Emitting Diode Design, *ACS Energy Lett.* 2023, **8**, 2395-2400.

[43] A. Satpathy, W.T. Huang, M.H. Chan, T.Y. Su, M. Kamiński, N. Majewska, S. Mahlik, G. Leniec, S.M. Kaczmarek, M. Hsiao and R.S. Liu, Near-Infrared I/II Nanophosphors with Cr^{3+}/Ni^{2+} Energy Transfer for Bioimaging, *Adv. Opt. Mater.*, 2023, **11**, 2300321.

[44] Q. Zhang, D. Liu, Z. Wang, P. Dang, H. Lian, G. Li and J. Lin, $LaMgGa_{11}O_{19}$: Cr^{3+}, Ni^{2+} as Blue-Light Excitable Near-Infrared Luminescent Materials with Ultra-Wide Emission and High External Quantum Efficiency, *Adv. Opt. Mater.*, 2023, **11**, 2202478.

[45] Y. Zhuo, F. Wu, Y. Niu, Y. Wang, Q. Zhang, Y. Teng, H. Dong, and Z. Mu, Super Broadband Emission Across NIR-I and NIR-II Under Blue Light Excitation of Cr^{3+}, Ni^{2+} Co-Doped Sr_2GaTaO_6 Phosphor Achieved by Two-Site Occupation and Effective Energy, *Laser & Photonics Rev.*, 2024, **18**, 2400105.

[46] Z. Chen, Y. Xiang, X. Qin, L. Zhong, H. Liao, S. Liu and M. Wu, Revealing energy

transfer mechanisms and accelerating intelligent detection: Cr^{3+} and Ni^{2+} co-doped $Lu_2CaMg_2Si_3O_{12}$ phosphors for NIR applications, *J. Mater. Chem. C.*, 2025. https://doi.org/10.1039/D5TC00476D

[47] G. Cai, T. Naillon, J. Seguin, D. Scherman, N. Mignet, C. Chaneac and B. Viana, ZGSO: Cr^{3+}, Ni^{2+} Persistent Phosphors with Dual Emission in NIR-I and SWIR Ranges for Bio-Imaging Applications, *Small.*, 2024, **20**, 2406507.

[48] Q. Zhang, G. Li, D. Liu, P. Dang, L. Qiu, H. Lian, M.S. Molokeev and J. Lin, Optical Thermometer Based on Efficient Near-Infrared Dual-Emission of Cr^{3+} and Ni^{2+} in Magnetoplumbite Structure, *Adv. Opt. Mater.*, 2023, **12**, 2301429.

[49] M. Tan, Y. Gao, J. Chen, X. Lu, B. Zhu, L. Huan and J. Qiu, A Nickel-doped, lanthanum gallium germanate-based phosphor as an ultra-broadband short-wavelength infrared region emitter for optical imaging, *Ceram. Int.*, 2024, **50**, 23685-23693.

[50] D. Wang, L. Yan, G. Zhu, S. Ma, N. Zhou, S. Li and B. Dong, Achieving flat ultra-broadband NIR emission in Cr^{3+} doped garnet-type phosphors enabled by structural regulation toward multi-functional spectroscopy applications, *Laser & Photonics Rev.*, 2025, **19**, 2401256.

[51] Y. Zhao, X. Wang, Q. Wang, T. Zhou, Y. Chen, J. Xu and R.J. Xie, Abnormal spectral broadening of ordered-structure near-infrared phosphor La_2CaHfO_6: Cr^{3+}, *J. Mater. Chem. C*, 2024, **12**, 10532-10539.

[52] M.D. Dramićanin, Ł. Marciniak, S. Kuzman, W. Piotrowski, Z. Ristić, J. Periša and C.G. Ma, Mn^{5+}-activated $Ca_6Ba(PO_4)_4O$ near-infrared phosphor and its application in luminescence thermometry, *Light Sci. Appl.*, 2022, **11**, 279.

[53] F. Zhu, Y. Gao and J. Qiu, Cr^{3+}-Doped $LiAlO_2$ NIR-I emitting phosphors with

superior resistance to thermal quenching for night vision monitoring and bioimaging, *ACS Appl. Mater. Interfaces*, 2024, **16**, 60599-60607.

[54] J. Sun, M. Jia, W. Xu, M. Wang and Z. Sun, Designing high thermally stable deep red phosphors based on low thermal expansion coefficients for optical applications, *Opt. Lett.*, 2024, **49**, 1504-1507.

[55] H. Yu, Z. Gao, H. Wang, S. Zhao, D. Deng and S. Xu, Zero-thermal-quenching broadband NIR-II emitting $Mg_4Nb_2O_9$: Ni^{2+} phosphor via defective engineering and multi-site occupation, *J. Alloys Compd.*, 2025, **1020**, 179519.

[56] A. Balhara, S. K. Gupta, B. Modak, A. K. Yadav, B. S. Naidu and K. Sudarshan, Broadband Shortwave Infrared-Emitting Cr^{3+}-and Ni^{2+}-Codoped $Y_3Al_2Ga_3O_{12}$ Phosphor with Excellent Thermal Stability for Multifunctional Applications, *ACS Appl. Mater. Interfaces.*, 2024, **17**, 1509-1521.

[57] Y. Li, Y. Lu, H. Ju, W. Wang, D. Tu, H. Lu and H. Zou, A High-Efficiency NIR-II Emitting $LiAlSiO_4$: Cr/Ni Phosphors through Violet Excitation for NIR pc-LED Application, *ACS Appl. Opt. Mater.*, 2024, **2**, 1933-1938.

[58] C. Gong, Z. Wang Z and J. Wang, A novel broadband near-infrared phosphor $NaBaScSi_2O_7$: Fe^{3+} and its application in pc-LED and night vision, *Sci. China Mater.*, 2025, **1**, 8.

[59] S. Yang, X. Xue and F. Jiang, A novel $KSrScSi_2O_7$: *x*Cr silicate phosphor, luminescence/chromaticity, and applications in NIR pc-LED and stable green ceramic pigments, *J. Rare Earths.*, 2025. https://doi.org/10.1016/j.jre.2024.12004